

## Rapid response in recovery time, humidity sensing behavior and magnetic properties of rare earth(Dy & Ho) doped Mn–Zn ceramics

A. El-Denglawey<sup>a, \*\*</sup>, K. Manjunatha<sup>b</sup>, E. Vijay Sekhar<sup>c</sup>, B. Chethan<sup>d</sup>, Jian Zhuang<sup>e</sup>, Jagadeesha Angadi V<sup>f,\*</sup>

<sup>a</sup> Department of Physics, College of University College at Turabah, Taif University, P.O. box 11099 Taif 21944, Saudi Arabia

<sup>b</sup> Department of Physics, School of Engineering, Presidency University, Bangalore-560064, India

<sup>c</sup> P.G. Department of Chemistry, J.S.S College for Women, Mysuru 570009, India

<sup>d</sup> Department of Physics, VTU Research Centre, JNN College of Engineering, Shivamogga-577204, India

<sup>e</sup> Electronic Materials Research Laboratory, Key Laboratory of the Ministry of Education & International Center for Dielectric Research, Xi'an Jiaotong University, Xi'an, 710049 China

<sup>f</sup> Department of Physics, P.C. Jabin Science College, Hubballi-580031, India



### ARTICLE INFO

#### Keywords:

Solution combustion method  
FTIR  
Humidity sensing  
Saturation magnetization

### ABSTRACT

In the present world, the development of room temperature humidity sensor materials has always been a very popular research field. Rare earth (RE) doped ferrites are considered as potential resistive humidity sensing material owing to its high remarkable surface morphology with high porosity. Recent studies have shown that ferrite ceramics have good response in recovery time and have excellent humidity sensing behavior. With this in mind, solution combustion synthesis was used to effectively prepare RE dysprosium ( $Dy^{3+}$ ) and holmium ( $Ho^{3+}$ ) doped Mn–Zn ferrite ceramics with the chemical formula  $Mn_{0.5}Zn_{0.5}Dy_xHo_yFe_{2-x}O_4$  ( $x = 0.005$  to  $0.03$ ) (MZDHF) (where  $x, y = 0.0, 0.01, 0.015, 0.02, 0.025$  and  $0.03$ ). The MZDHF XRD pattern revealed the purity of the samples without any secondary phase. The crystallite size MZDHF is in the nano range. Further, the calculated lattice parameter of MZDHF is found to be increasing with the RE content. The two prominent major absorption bands related to A-site and B-site were confirmed by FTIR spectra. The hysteresis loops of MZDHF are used to investigate the differences in magnetic properties with an  $Dy^{3+}$ - $Ho^{3+}$  concentration. The remanence magnetization, saturation magnetization, coercivity and anisotropy of the ferrites were determined. The saturation magnetization decreases with increase of  $Dy^{3+}$ - $Ho^{3+}$  concentration. The change in the surface resistance for all the samples was studied. Among all the samples,  $Mn_{0.5}Zn_{0.5}Dy_{0.03}Ho_{0.03}Fe_{1.96}O_4$  composite has shown a drastic variation in resistance. And the corresponding sensing response for the same sample is found to be 99%. Along with this, the sample has shown a least hysteresis and good stability. Also, the  $Mn_{0.5}Zn_{0.5}Dy_{0.03}Ho_{0.03}Fe_{1.96}O_4$  composite has shown a good timing behavior of 90 s and 18 s. The sensing mechanism for the prepared  $Mn_{0.5}Zn_{0.5}Dy_{0.03}Ho_{0.03}Fe_{1.96}O_4$  composite was thoroughly discussed.

### 1. Introduction

Nano-ferrites, which are currently being studied, have piqued curiosity on account of their remarkable magnetic and sensing properties. Due to their extraordinary physical and chemical properties, spinel ferrites nanoparticles have become a significant field of research in nanotechnology, nanoscience, and nanoelectronics [1–6]. Spinel ferrites nanoparticles are important materials in ferrofluid technology and data storage devices [7,8]. Their applications also span almost every aspect of

everyday life, including energy-related applications, medical diagnosis, photocatalysis and magnetic recording systems [9,10]. Science and innovation nowadays rely heavily on sensing devices and materials. Humidity sensor systems have a wide range of possible applications, including medicine, chemical gas purification, agriculture, garment manufacturing, and food packaging [11,12]. Ceramics, polymers, and organic compounds can all be used to make humidity sensor materials. With high stability and low hysteresis, sensing materials help their sensing response and recovery time. Ceramic-based materials are

\* Corresponding author.

\*\* Co-corresponding author;

E-mail addresses: [a.denglawey@tu.edu.sa](mailto:a.denglawey@tu.edu.sa), [denglawey@yahoo.com](mailto:denglawey@yahoo.com) (A. El-Denglawey), [jagadeeshangadiv@gmail.com](mailto:jagadeeshangadiv@gmail.com) (J. Angadi V).

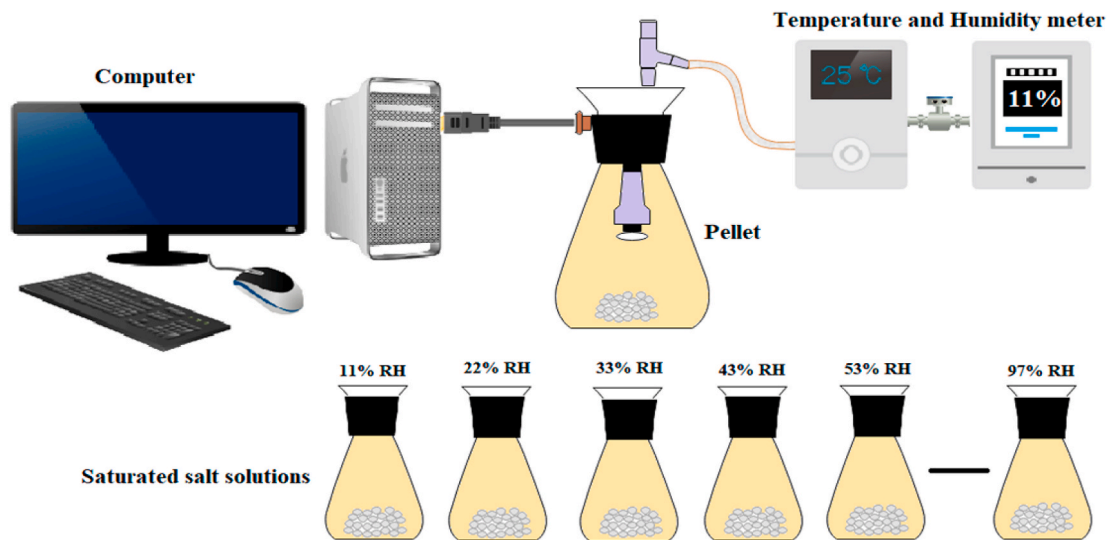


**Fig. 1.** Schematic representation of Humidity sensing set-up.

discovered to be a preferred option over any remaining sensing materials due to their high mechanical power, mechanical and chemical stability and low cost [13–15]. The spinel ferrites have a general formula  $AB_2O_4$ , where A and B denote the tetrahedral site and octahedral site, respectively [16,17]. The general empirical formula for spinel ferrites is  $MFe_2O_4$ , where M is the divalent (+2) metal ions such as  $Mn^{2+}$ ,  $Zn^{2+}$ ,  $Co^{2+}$ ,  $Mn^{2+}$ ,  $Ni^{2+}$ ,  $Mg^{2+}$  and so on [18,19]. Almost all properties of spinel ferrites nanoparticles are tailored by the careful selection of metal ions and their distribution between A-sites and B-sites. Since then, some ferrites have been prepared using numerous methods such as solution combustion method, co-precipitation, sonochemical method, micro-emulsion, and so on [20–23]. Spinel ferrites are extensively researched for their significant applications in the electronics field like sensors, memory devices, data storage, inductors, power conversion, high-frequency materials and also in the biosciences field like purification, contrast agents, drug delivery systems and biomolecule separation [24–29]. The spinel family includes Mn-Zn ferrite, a soft magnetic substance of high saturation induction, low coercivity and high magnetic permeability. It also has a small hysteresis loop, low magnetic losses, and low eddy-current losses, in addition to a variety of applications in medical diagnosis, drug delivery, and heat transfer [30–32]. Mn-Zn ferrites are additionally significant in industry in view of their excellent magnetic properties, such as low magnetic loss and high initial magnetic permeability [33–35].

Since magnetic permeability is proportionate to saturation magnetization ( $M_s$ ) square and coercive fields ( $H_c$ ) is inversely proportionate to saturation magnetization ( $M_s$ ), high saturation magnetization is likewise one of the crucial obligations for magnetic soft materials to save energy and achieve system miniaturization. Unfortunately, due to their ferrimagnetism, Mn-Zn ferrites have a low  $M_s$ . Ions substitution is commonly used in the synthesis of Mn-Zn ferrites to improve the  $M_s$ . The improvement is, however, restricted [36–39]. In the current work, the  $Mn_{0.5}Zn_{0.5}Dy_xHo_yFe_{2-x}O_4$  ( $x = 0.005$  to  $0.03$ ) NPs were synthesized by solution combustion method. Synthesized nanoparticles were studied through XRD, FTIR, VSM and humidity sensing studies to investigate the structural, magnetic and sensing properties.

## 2. Synthesis method and characterizations

Stoichiometric quantities of oxidizers such as manganese nitrate, zinc nitrate, ferrous nitrate, dysprosium nitrate, holmium nitrate and fuels as stoichiometry quantities of fuels glucose and urea were mixed in 30 ml of distilled water, and the combined solution was taken in a glass

beaker. Then the combined solution was continuously stirred for 1 h to achieve a homogeneous solution. At  $450\text{ }^{\circ}\text{C}$ , this homogeneous solution was kept in a box style muffle furnace that had been preheated. The solution boils, froths, and then burns with a smoldering flame at first. The combustion process will be completed within 20 min.

The XRD was characterized by utilizing  $\text{CuK}_{\alpha}$  radiation ( $\lambda = 1.5406\text{ \AA}$ ) and the  $2\theta$  diffractogram was run from  $10^{\circ}$  to  $80^{\circ}$  with a stage size of 0.02°. We can deduce crystalline phase and structure from XRD patterns. The vibration modes of the sample were estimated using FTIR spectra (IR-100 Shimadzu) in the range of 4000 to 400  $\text{cm}^{-1}$ . A PPMS, Quantum Design Inc. Device was utilized to study the magnetic properties at room temperature.

### 2.1. Humidity sensing set-up

The pellet of the sample was prepared using a hydraulic press to perform the humidity sensing studies. The silver was pasted on it to get the electrical contact and heated in an oven for 2 h at  $55\text{ }^{\circ}\text{C}$ . The prepared sample was placed within the probes of the electrode. The ends of the electrode were connected to the digital multimeter and interfaced with the computer to measure the resistance by using AC mode. Each resistance value was determined by enclosing the pellet in the electrode in each flask containing a different saturated salt solution [40]. The schematic humidity setup was represented in Fig. 1.

## 3. Results

### 3.1. Structural analysis

The X-ray diffractometer (XRD) is a well-known instrument for investigating the structure of prepared materials. Fig. 2 shows the refined XRD pattern of MZDHF. The single-phase cubic structure was verified for all samples, and the pattern matched data card ICDD#10–0319 perfectly. The miller indices (hkl) suggested a spinel cubic structure without the appearance of secondary phases (Fig. 3). The lattice constant (a) values were estimated from Rietveld refinement. For  $x = y = 0.005$  to  $0.03$  concentration, the values of 'a' were found 8.3964 to 8.4245  $\text{\AA}$ , respectively (see Table 1). Equation (1) was utilized to estimate the crystallite size of MZDHF using the Debye Scherrer equation [41,42];

$$D = k \frac{\lambda}{\beta \cos \theta}$$

The "λ" denotes the X-ray wavelength, the "β" denotes the FWHM

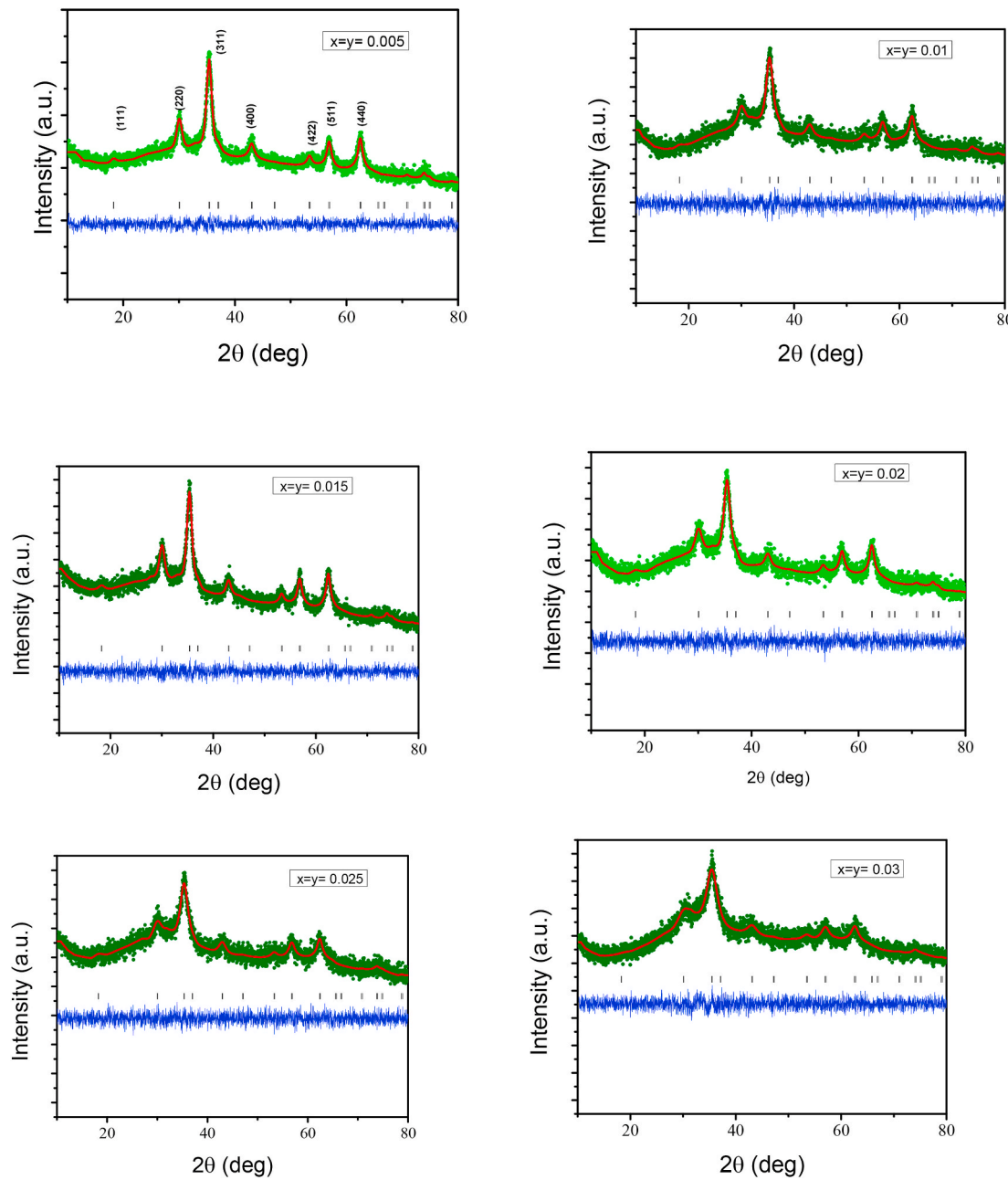


Fig. 2. The XRD patterns of  $\text{Mn}_{0.5}\text{Zn}_{0.5}\text{Dy}_x\text{Ho}_{1-x}\text{O}_4$  ( $x = y = 0.005$  to  $0.03$ ) nanoparticles.

value,  $k$  is the Scherrer constant and  $\theta$  denotes the diffraction angle. The crystallite sizes measured ranged from 11.88 to 6.44 nm for  $x = 0.005$  to  $0.03$ , respectively. The large ionic radius of rare-earth ions increases the lattice parameter value while decreasing the average crystallite size, which is a popular trend [43]. However, in some cases, such as in our investigation, the researchers found different actions. The introduction of the  $\text{Dy}^{3+}$ - $\text{Ho}^{3+}$  ions cause increases in the lattice parameter in our analysis. As the large ionic radius of  $\text{Dy}^{3+}$  (0.912 Å) and  $\text{Ho}^{3+}$  (0.901 Å) ions replaces the small ionic radius of  $\text{Fe}^{3+}$  (0.645 Å) ion at the B-site position, the lattice structure becomes asymmetric [44].

### 3.2. FTIR analysis

In FTIR spectra, spinel ferrites are characterized by two strong bands of Metal-Oxygen (M O). The higher frequency band  $\nu_1$  related to A-site (tetrahedral site) stretching vibrations in the  $600$ - $500 \text{ cm}^{-1}$  range, while the lower frequency band  $\nu_2$  related to B-site (octahedral site) stretching

vibration in the  $500$ - $400 \text{ cm}^{-1}$  range. Fig. 3 shows the FTIR spectra of MZDHF. These spectra were taken in the  $380$ - $4000 \text{ cm}^{-1}$  wavenumber range. Both vibrational frequencies such as  $\nu_1$  and  $\nu_2$  for  $\text{Dy}^{3+}$ - $\text{Ho}^{3+}$  doped samples showed a steady shift to the lower frequencies side with increasing of  $\text{Dy}^{3+}$ - $\text{Ho}^{3+}$  concentration, as shown in the spectra. The following is a breakdown of how the bands are shifting. The addition of  $\text{Dy}^{3+}$ - $\text{Ho}^{3+}$  ions to B-sites (octahedral sites) causes  $\text{Mn}^{2+}$ - $\text{Zn}^{2+}$  ions to migrate to A-sites [44]. This will unwind the strain by transporting  $\text{Fe}^{3+}$  ions from A-site to B-site. The strong ionic radii of tetrahedral sites are due to the enhanced dwelling of  $\text{Mn}^{2+}$ - $\text{Zn}^{2+}$  ions. Similarly,  $\text{Dy}^{3+}$ - $\text{Ho}^{3+}$  ions content increasing at octahedral sites results in enhanced ionic radii at octahedral sites. Actually, these migrations cause an increase in the ionic radii of the A-site and B-site, resulting in a gradual shifting of vibrational frequencies i.e.,  $\nu_1$  and  $\nu_2$  to lower frequencies side [45].

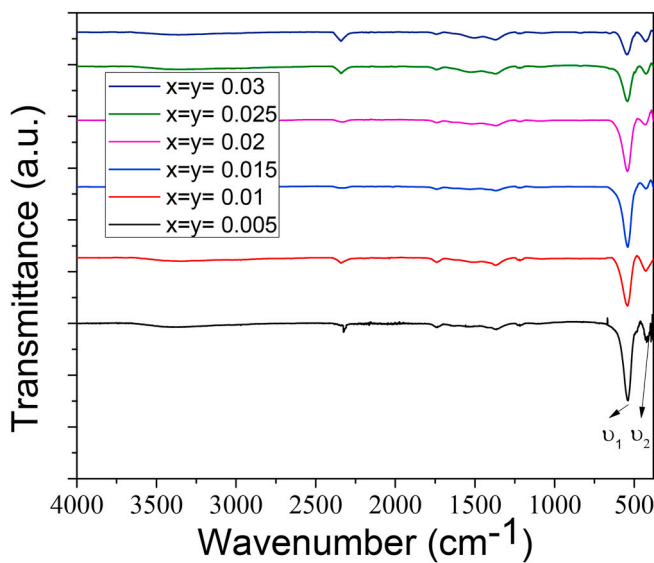


**Fig. 3.** FTIR spectra of  $Mn_{0.5}Zn_{0.5}DyxHoFe_{2-x}O_4$  ( $x = y = 0.005$  to  $0.03$ ) nanoparticles.

**Table 1**  
Structural parameters of  $Mn_{0.5}Zn_{0.5}DyxHoFe_{2-x-y}O_4$  ( $x = y = 0.005$  to  $0.03$ ) nanoparticles.

Dy-Ho content	Lattice parameters (Å)	Crystallite Size D in (nm)	Volume (Å³)	Hopping length (Å)	
				$L_A$	$L_B$
$x = 0.005$	8.3964	11.88	591.94	3.6357	2.9685
$x = 0.01$	8.4044	10.65	593.63	3.6392	2.9714
$x = 0.015$	8.4067	8.001	594.12	3.6402	2.9722
$x = 0.02$	8.4157	7.80	596.03	3.6441	2.9753
$x = 0.025$	8.4193	7.97	596.79	3.6456	2.9766
$x = 0.03$	8.4245	6.64	597.90	3.6479	2.9785

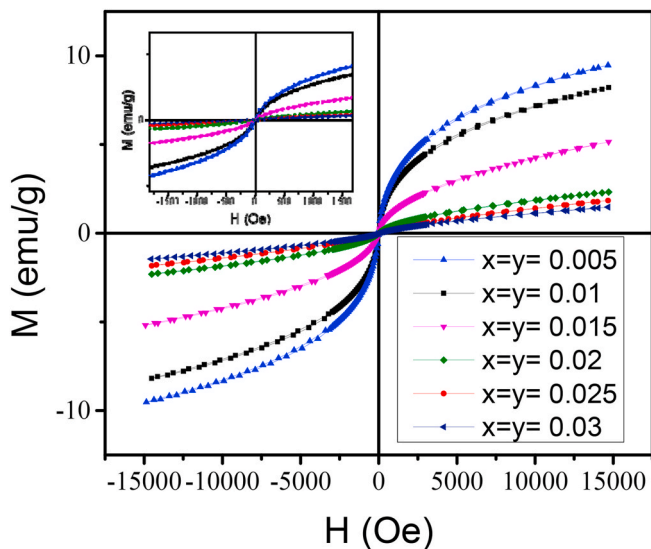


**Fig. 4.**  $M - H$  loop of  $Mn_{0.5}Zn_{0.5}DyxHoFe_{2-x}O_4$  ( $x = y = 0.005$  to  $0.03$ ) nanoparticles.

### 3.3. Magnetic study

Magnetic hysteresis loops for all samples calibrated at room temperature with an applied magnetic field of 15000 Oe are shown in Fig. 4.

**Table 2**

The magnetic parameters,  $M_s$  (saturation magnetization),  $M_r$  (remanent magnetization),  $S$  (reduced remanence),  $H_c$  (coercivity),  $K_c$  (cubic anisotropy) and  $K_u$  (uniaxial anisotropy).

Dy-Ho content	$M_s$ (emu/g)	$M_r$ (emu/g)	$S$	$H_c$ (Oe)	$K_c$ (erg/Oe)	$K_u$ (erg/Oe)
$x = 0.005$	6.362	0.1318	0.0207	16.24	161.43	104.89
$x = 0.01$	5.945	0.1285	0.0216	18.2	169.06	109.84
$x = 0.015$	2.386	0.0465	0.0194	16.43	61.25	39.79
$x = 0.02$	0.797	0.0138	0.0173	16.56	20.62	13.39
$x = 0.025$	0.652	0.0068	0.0104	14.96	15.24	9.90
$x = 0.03$	0.507	0.0053	0.0104	15.23	12.06	7.83

With enhancing Ho-Dy doping, the  $M_s$  (saturation magnetization) clearly decreased. The saturation magnetization values for all the samples were calculated as follows: a straight line was extrapolated towards the magnetization axis from the linear region of the magnetization curve. The saturation magnetization was calculated as the crossing point of this line with the magnetization axis. Table 2 shows the  $M_s$  values for all of the samples. A maximum saturation magnetization value was obtained for the  $x = y = 0.005$  sample, indicating the existence of superparamagnetic and single-domain particles [46]. The values of  $M_s$  in the Ho-Dy doped samples were found to decrease even more as the Ho-Dy content increased. This reduction in saturation magnetization values may be identified with the decreasing size with increase of Dy-Ho content, as shown by the XRD results (Table 2). Besides, the 4f electrons of  $Ho^{3+}$  and  $Dy^{3+}$  ions have no exchange contact with 3d electrons of  $Fe^{3+}$  ions. As a result, at room temperature, the magnetic moments (magnetic dipoles) of  $Ho^{3+}$  and  $Dy^{3+}$  ions, originating from the 4f electrons are arbitrarily focused. They are isolated and occupy the B site as “paramagnetic-like-defect” atoms [47,48]. The coercivity varies with  $Dy^{3+}$ - $Ho^{3+}$  concentration. Table 2 shows the  $M_r$  (remanent magnetization) values obtained from the  $M - H$  loop's intercept on the magnetization axis. The remanent magnetization values decrease with the increase of  $Dy^{3+}$ - $Ho^{3+}$  concentration in the samples, as can be seen [46]. The sample with 0.03 mol% doped  $Dy^{3+}$ - $Ho^{3+}$  sample had the lowest remanent magnetization value, indicating that the sample has “higher” superparamagnetic-like behavior due to a minor doping of the  $Dy^{3+}$ - $Ho^{3+}$  ions [47]. The uniaxial and cubic anisotropy values were estimated and tabulated in Table 2.

### 3.4. Humidity sensing studies

The variation in the surface resistance with different humidity was depicted in Fig. 5. MZDHF was tested for the humidity sensing behavior at the room temperature. The variation in the resistance was maximum for the highest composition sample. It is noteworthy that, as the content of the dopants increases, the resistance variation enhances and the humidity sensing response goes on increase. The sensing response ( $S_R$ ) for all the samples was calculated using equation (2).

$$S_R = \frac{|R_L - R_H|}{R_L} \times 100\% \quad (2)$$

where,  $R_L$  is the resistance at lower % RH and  $R_H$  are the resistance at higher % RH.

The variation in the sensing response with the % RH of all the composites is represented in Fig. 6. As the dopants increases, the linear variation in the resistance increases. In turn, the sensing response increases. For the highest composition, the sensing response has reached the epitome of 99%. The bar graphs show the increase in the sensing response for each relative humidity clearly. The crystallite has decreased, leading to the improvement in porosity and an increase in the surface area, which provides more active sites for the water adsorption, which helps for the enhancement in the humidity sensing behavior [49]. Since the highest composition sample has shown the maximum variation

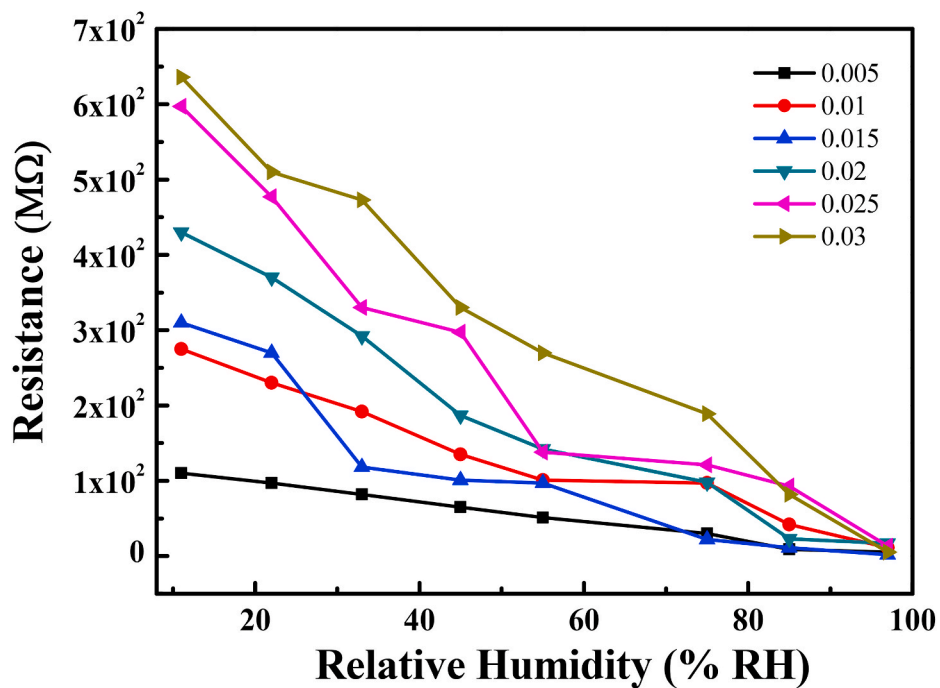


Fig. 5. Variation of resistance with the % RH.

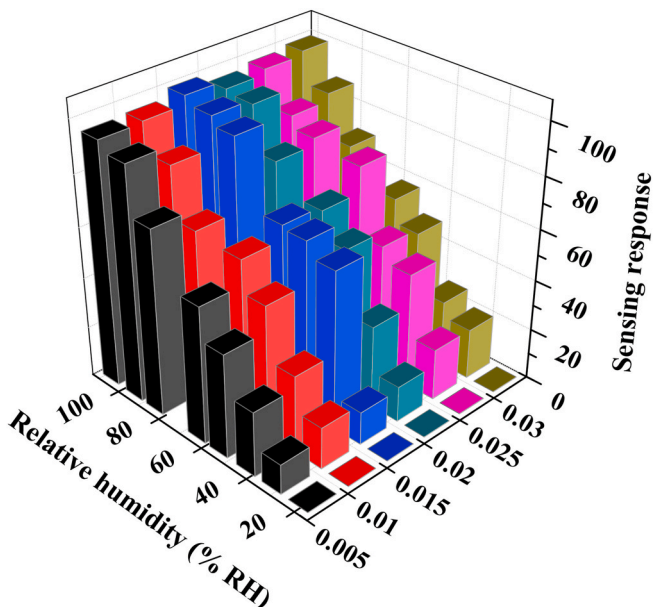


Fig. 6. Variation of Sensing response with the % RH.

in the resistance and the sensing response is good. Thus, the other humidity sensing parameters were performed only for the highest composition sample.

#### 3.4.1. Timing behavior

The response and recovery behavior for the  $Mn_{0.5}Zn_{0.5}Dy_{0.03}Ho_{0.03}Fe_{1.96}O_4$  composite was shown Fig. 7. For the measurement of the timing behavior two flasks with lower of 11% RH and higher humidity of 97% RH was considered. The holder containing the testing sample was places in the flask at 11% RH, with in the time gap of 1 s suddenly the sample was moved to the flask containing 97% RH. The response time was recorded by moving the sample from 11% RH to 97% RH and the recovery time was recorded by moving the

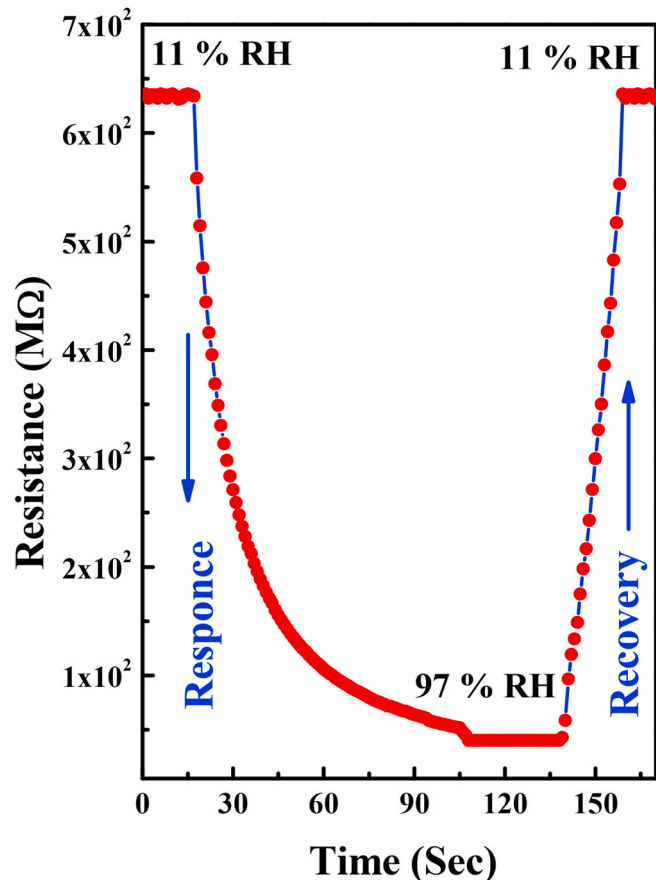


Fig. 7. Humidity response and recovery behavior of the composite.

sample from 97% RH to 11% RH, then the response and the recovery time was recorded. Since the increase's porosity and larger surface area the highest composition sample has shown a response time was found to

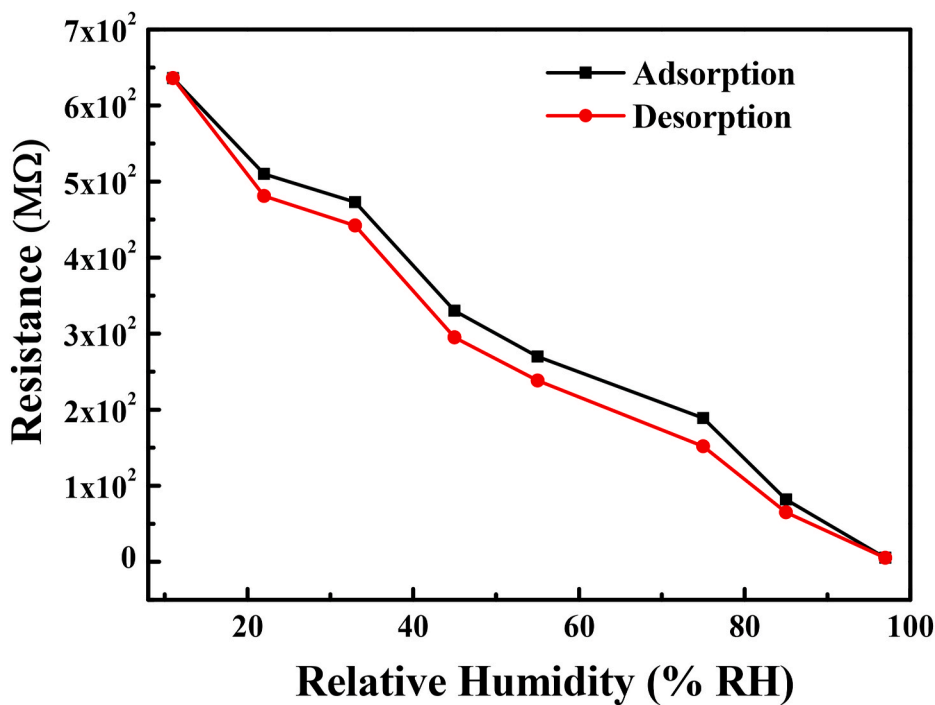


Fig. 8. Humidity adsorption and desorption behavior of the composite.

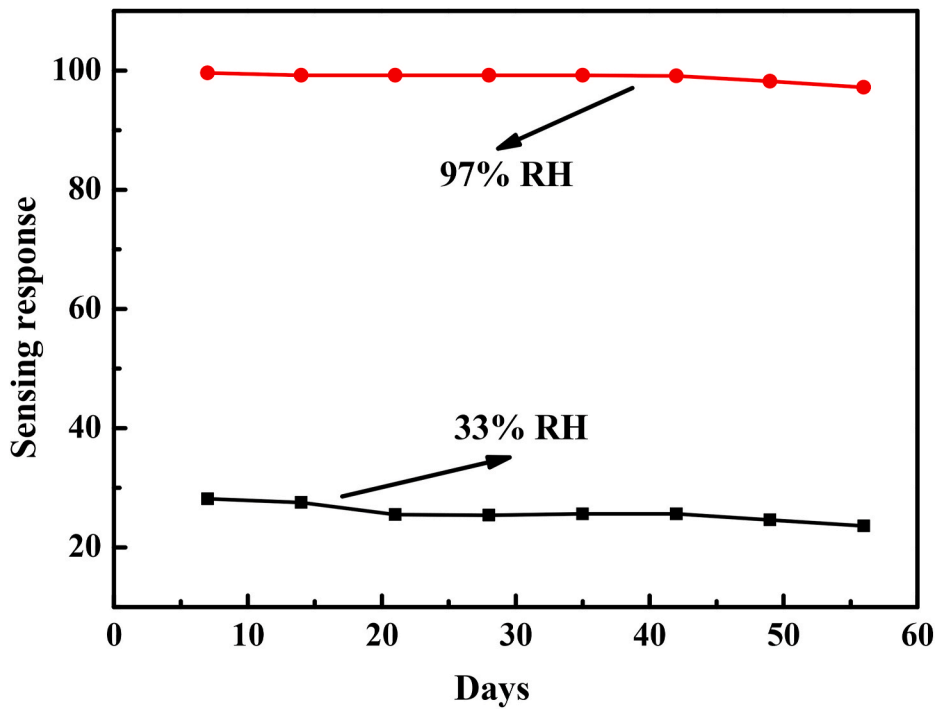


Fig. 9. Humidity sensing stability of the composite.

be 90 s and the recovery time recorded to be 18 s. It is noteworthy that, as the composition of the dopants increases the surface sites for the water adsorption increases in turn helps for humidity sensing [50].

#### 3.4.2. Humidity hysteresis

The variation in the absorption and desorption behavior of the composition is considered as the humidity hysteresis. The humidity hysteresis for the higher composition of the sample was shown in Fig. 8. The humidity hysteresis can be calculated by using Equation (3) [51].

The humidity hysteresis was calculated using Eq. (3),

$$\% \text{ Hysteresis} \equiv \left[ \frac{(Y_{ab} - Y_{ac})}{(Y_{min} - Y_{max})} \times 100\% \right] \quad (3)$$

where,  $Y_{ab}$  and  $Y_{ac}$  are the highest and least value of  $Y$  at the mean of the %RH. The humidity hysteresis was found to be 9% for the highest composition sample.

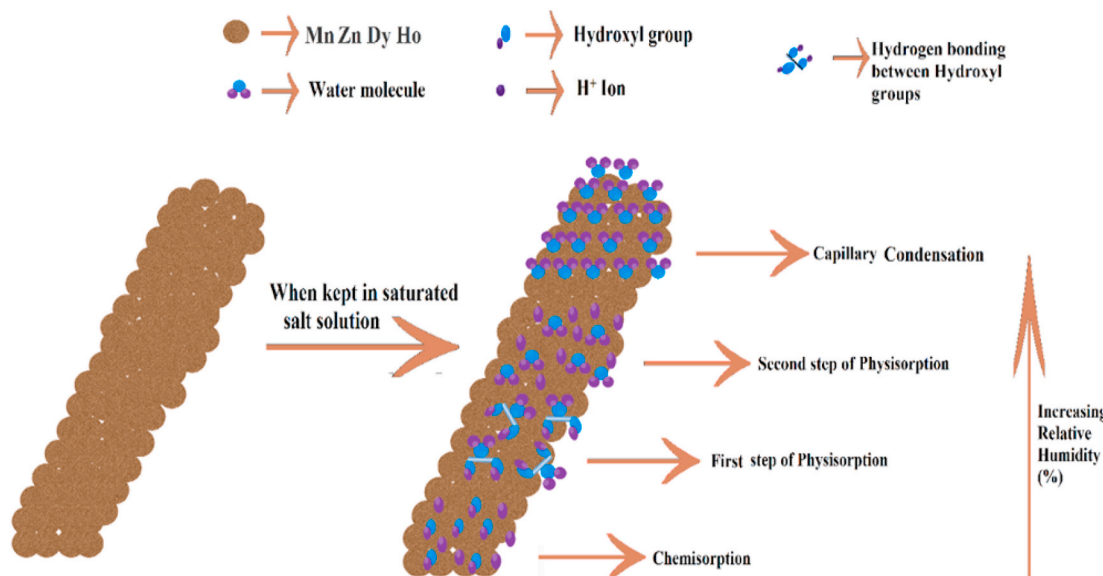


**Fig. 10.** The Humidity sensing mechanism.

#### 3.4.3. Humidity stability

Stability is the most important parameter to judge the potentiality of the sensor. For every one weak the sensing response of the sample was measured for 33% and 97% RH. The humidity stability for the sample was given in Fig. 9. The standard deviation for the 33% RH was 0.29 and for the 97% RH it was found to be 0.42. This represents that at lower humidity the sensor was more stable and efficient [52].

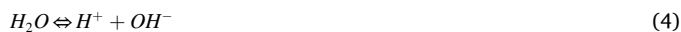
The enhanced variation in the surface resistance, humidity sensing response, good response and recovery behavior, least hysteresis and more stability make this sensor more potential and can be used for larger production.

#### 3.4.4. Humidity sensing mechanism

The sensing mechanism can be analyzed in to 3 steps:

1. Chemisorption,
2. Physisorption and
3. Condensation [53].

Rare earth metals (Dy & Ho) brings the porosity in the ceramic material and increases the surface to volume ratio (see Fig. 10). These critters help in the hopping of the protons on the surface and increase the conductivity, intern helps in enhancing the humidity sensing response. In the beginning of the first step, due to strong charge density the water molecule undergoes dissociation to for  $H^+$  and  $OH^-$  ions [11,54].



As the amount of water content increases, the hydroxyl ions adsorb on the active site, forming the chemisorbed layer. As the relative humidity further enhances, the two hydroxyl ions make the H-bond with the one water molecule forming bulk water [55]. The bulk water is more unstable in nature; thus, it undergoes ionization to form water and an  $H^+$  ion. Due to the release of the  $H^+$  ions the conductivity becomes maximum. This prompted the development of the first physisorbed layer.



At the last stage, many more water molecules pile up to form the second physisorbed layers [56]. At this point, many  $H_2O$  molecules have entered the pores, and intergranular defects and vacancy sites

create a path for protons to hop easily on the sample's surface. Prompting expansion in the conductivity [57].

#### 4. Conclusion

The  $Dy^{3+}$ - $Ho^{3+}$  doped Mn-Zn ferrite NPs have been synthesized by solution combustion method with glucose and carbamide as fuels. The XRD pattern of all synthesized samples revealed the spinel cubic structure. The lattice constant of all samples was found to be 8.4964 to 8.4245 Å. The lattice constant increases with  $Ho^{3+}$ - $Dy^{3+}$  concentration due because of the large ionic radius of  $Dy^{3+}$  (0.912 Å) and  $Ho^{3+}$  (0.901 Å) ions replaces the small ionic radius of  $Fe^{3+}$  (0.645 Å) ion at the B-site position. The two major absorption bands related to A-site and B- site were studied using FTIR spectra and it affirms the development of spinel ferrite. The hysteresis loops of MZDHF were used to investigate the differences in magnetic properties with  $Dy^{3+}$ - $Ho^{3+}$  concentration. The saturation magnetization and remanent magnetization decreases with an increase of  $Dy^{3+}$ - $Ho^{3+}$  concentration. A maximum saturation magnetization value was obtained for the  $x = y = 0.005$  sample, indicating the existence of superparamagnetic and single-domain particles. The humidity sensing performance of all the samples was studied. Among all the samples,  $Mn_{0.5}Zn_{0.5}Dy_{0.03}Ho_{0.03}Fe_{1.96}O_4$  composite has shown a drastic variation in the resistance with best sensing behavior. The sensor proved its potential by showing least hysteresis, good stability and good timing behavior. Thus, the sensor can be used for industrial applications and humidity monitoring systems.

#### Declaration of competing interest

The authors declare that they have no known competing financial interests or personal relationships that could have appeared to influence the work reported in this paper.

#### Acknowledgment

Taif University Researchers Supporting Project Number(TURSP-2020/45) Taif University, Taif, Saudi Arabia.

#### References

- [1] J. Judith Vijaya, G. Sekaran, M. Bououdina, Effect of  $Cu^{2+}$  doping on structural, morphological, optical and magnetic properties of  $MnFe_2O_4$  particles/sheets/flakes-like nanostructures, Ceram. Int. 41 (2015) 15–26.

- [2] X. Meng, H. Li, J. Chen, L. Mei, K. Wang, X. Li, Mössbauer study of cobalt ferrite nanocrystals substituted with rare-earth  $Y^{3+}$  ions, *J. Magn. Magn Mater.* 321 (2009) 1155–1158.
- [3] S. Amiri, H. Shokrollahi, The role of cobalt ferrite magnetic nanoparticles in medical science, *Mater. Sci. Eng. C* 33 (2013) 1–8.
- [4] J. Popplewell, L. Sakhnini, The dependence of the physical and magnetic properties of magnetic fluids on particle size, *J. Magn. Magn Mater.* 149 (1995) 72–78.
- [5] K. Raj, B. Moskowitz, R. Casciaro, Advances in ferrofluid technology, *J. Magn. Magn Mater.* 149 (1995) 174–180.
- [6] K. Manjunatha, I.C. Sathish, S.P. Kubrin, A.T. Kozakov, T.A. Lastovina, A. V. Nikolskii, K.M. Srinivasamurthy, Mahaboob Pasha, V. Jagadeesha Angadi, X-ray photoelectron spectroscopy and low temperature Mössbauer study of  $Ce^{3+}$ -substituted  $MnFe_2O_4$ , *J. Mater. Sci. Mater. Electron.* 30 (2019) 10162–10171.
- [7] P.D. Thang, G. Rijnders, D.H.A. Blank, Spinel cobalt ferrite by complexometric synthesis, *J. Magn. Magn Mater.* 295 (2005) 251–256.
- [8] I.C. Sathish, K. Manjunatha, V. Jagadeesha Angadi, Ranjith kumar reddy, structural, microstructural, electrical, and magnetic properties of  $CuFe_{2-(x+y)}Eu_xSc_yO_4$  (where x and y vary from 0 to 0.03) nanoparticles, *J. Supercond. Nov. Magnetism* 33 (2020) 3963–3973.
- [9] M.Y. Lodhi, K. Mahmood, A. Mahmood, H. Malik, M.F. Warsi, I. Shakir, M. Asghar, M.A. Khan, New  $Mg_0.5Co_0.5-xFe_2O_4$  nano-ferrites: structural elucidation and electromagnetic behavior evaluation, *Curr. Appl. Phys.* 14 (2014) 716–720.
- [10] M.M. Rashad, R.M. Mohamed, H. El-Shall, Magnetic properties of nanocrystalline Sm-substituted  $CoFe_2O_4$  synthesized by citrate precursor method, *J. Mater. Process. Technol.* 198 (2008) 139–146.
- [11] I.C. Sathisha, K. Manjunatha, Bajorek Anna, B. Rajesh Babu, B. Chethan, T. Ranjith Kumar Reddy, Y.T. Ravikiran, V. Jagadeesha Angadi, Enhanced humidity sensing and magnetic properties of bismuth doped copper ferrites for humidity sensor applications, *J. Alloys Compd.* 848 (2020) 156577.
- [12] D. Zhang, D. Wang, P. Li, X. Zhou, X. Zong, G. Dong, Facile fabrication of high-performance QCM humidity sensor based on layer-by-layer self-assembled polyaniline/graphene oxide nanocomposite film, *Sensor. Actuator. B Chem.* 225 (2018) 1869–1877.
- [13] V. Jagadeesha Angadi, H.R. LakshmiPrasanna, K. Manjunatha, Investigation of structural, microstructural, dielectrical and magnetic properties of  $Bi^{3+}$ -doped manganese spinel ferrite nanoparticles for photonic applications, in: Bismuth - fundamentals and photonic applications, Intech Open publication, London, 2020, pp. 140–151.
- [14] D. Li, Y. Li, F. Li, J. Zhang, X. Zhu, S. Wen, S. Ruan, Humidity sensing properties of  $MoO_3-NiO$  nanocomposite materials, *Ceram. Int.* 41 (2015) 4348–4353.
- [15] J. Shah, R.K. Kotnala, B. Singh, H. Kishan, Microstructure-dependent humidity sensitivity of porous  $MgFe_2O_4-CeO_2$ , ceramic, *Sensor. Actuator. B Chem.* 128 (2007) 306–311.
- [16] M. Azhar Khan, M. Sabir, A. Mahmood, M. Asghar, K. Mahmood, M. Afzal Khan, I. Ahmad, M. Sher, M. Farooq Warsi, High frequency dielectric response and magnetic studies of  $Zn_{1-x}Tb_xFe_2O_4$  nanocrystalline ferrites synthesized via microemulsion technique, *J. Magn. Magn Mater.* 360 (2014) 188–192.
- [17] L. Kumar, M. Kar, Effect of  $La^{3+}$  substitution on the structural and magnetocrystalline anisotropy of nanocrystalline cobalt ferrite ( $CoFe_{2-x}La_xO_4$ ), *Ceram. Int.* 38 (2012) 4771–4782.
- [18] R.-R. Gao, Y. Zhang, W. Yu, R. Xiong, J. Shi, Superparamagnetism and spin-glass like state for the  $MnFe_2O_4$  nano-particles synthesized by the thermal decomposition method, *J. Magn. Magn Mater.* 324 (2012) 2534–2538.
- [19] C. Behera, R.N.P. Choudhary, P.R. Das, Size dependent electrical and magnetic properties of mechanically-activated  $MnFe_2O_4$  nanoferrite, *Ceram. Int.* 41 (2015) 13042–13054.
- [20] K.M. Srinivasamurthy, K. Manjunatha, E.I. Sitalo, S.P. Kubrin, I.C. Sathish, S. Mattepanavar, B. Rudraswamy, V.J. Angadi, Effect of  $Ce^{3+}$  substitution on the structural, morphological, dielectric, and impedance spectroscopic studies of Co-Ni ferrites for automotive applications, *Indian J. Phys.* 94 (2020) 593–604.
- [21] C. Ravikumar, R. Bandyopadhyaya, Mechanistic study on magnetite nanoparticle formation by thermal decomposition and coprecipitation routes, *J. Phys. Chem. C* 115 (2011) 1380–1387.
- [22] M.M. Baig, M.A. Yousuf, P.O. Agboola, M.A. Khan, I. Shakir, M.F. Warsi, Optimization of different wet chemical routes and phase evolution studies of  $MnFe_2O_4$  nanoparticles, *Ceram. Int.* 45 (2019) 12682–12690.
- [23] B.J. Palla, D.O. Shah, P. Garcia-Casillas, J. Matutes-Aquino, Preparation of nanoparticles of barium ferrite from precipitation in microemulsions, *J. Nanoparticle Res.* 1 (1999) 215–221.
- [24] D.L. Leslie-Pelecky, R.D. Rieke, Magnetic properties of nanostructured materials, *Chem. Mater.* 8 (1996) 1770–1783, <https://doi.org/10.1021/cm960077f>.
- [25] M.A. Radmanesh, S.A. Seyyed Ebrahimi, Synthesis and magnetic properties of hard/soft  $SrFe_{12}O_{19}/Ni_{0.7}Zn_{0.3}Fe_2O_4$  nanocomposite magnets, *J. Magn. Magn Mater.* 324 (2012) 3094–3098.
- [26] M.K. Surendra, S. Kanti De, M.S.R. Rao, Application worthy SPIONs: coated magnetic nanoparticles, *IEEE Trans. Magn.* 50 (2014) 2–7.
- [27] G.C. Papaefthymiou, Nanoparticle magnetism, *Nano Today* 4 (2009) 438–447.
- [28] F. Arteaga-Cardona, E. Gutiérrez-García, S. Hidalgo-Tobón, C. López-Vasquez, Y. A. Brito-Barrera, J. Flores-Tochihuitl, A. Angulo-Molina, J.R. Reyes-Leyva, R. González-Rodríguez, J.L. Coffer, U. Pal, M.P.-P. Diaz-Conti, D. Platas-Neri, P. Dies-Suarez, R.S. Fonseca, O. Arias-Carrión, M.A. Méndez-Rojas, Cell viability and MRI performance of highly efficient polyol-coated magnetic nanoparticles, *J. Nanoparticle Res.* 18 (2016) 345.
- [29] P. Poddar, J.L. Wilson, H. Srikanth, S.A. Morrison, E.E. Carpenter, Magnetic properties of conducting polymer doped with manganese-zinc ferrite nanoparticles, *Nanotechnology* 15 (2004) S570–S574.
- [30] S. Liu, L. Wang, K. Chou, Synthesis of metal-doped Mn-Zn ferrite from the leaching solutions of vanadium slag using hydrothermal method, *J. Magn. Magn Mater.* 449 (2017) 49–54.
- [31] M. Abhishek, K. Manjunatha, V. Jagadeesha Angadi, E. Melagiriyappa, B. N. Anandaram, H.S. Jayanna, M. Veena, K. Swaroop Acharya, Structural and magnetic properties of  $Eu^{3+}$ -substituted Mg-Cd nanoferrites: a detailed study of influence of high energy  $\gamma$ -rays irradiation, *Chem. Data Collect.* 28 (2020) 100460.
- [32] K. Hayash, M. Nakamura, W. Sakamoto, Y. Yogo, H. Miki, S. Ozaki, M. Abe, T. Matsumoto, K. Ishimura, Superparamagnetic nanoparticle clusters for cancer theranostics combining magnetic resonance imaging and hyperthermia treatment, *Theranostics* 3 (2013) 366.
- [33] M. Drofenik, A. Znidarsic, I. Zajc, Highly resistive grain boundaries in doped MnZn ferrites for high frequency power supplies, *J. Appl. Phys.* 82 (1997) 333.
- [34] B.P. Rao, B. Dhanalakshmi, S. Ramesh, et al., Cation distribution of Ni-Zn-Mn ferrite nanoparticles, *J. Magn. Magn Mater.* 456 (2018) 444.
- [35] V. Tsakaloudi, V. Zaspalis, A new Mn-Zn ferrite for high-speed data transmission applications in telecommunication networks, *J. Magn. Magn Mater.* 310 (2007) 2540.
- [36] S. Chikazumi, Physics of Ferromagnetism, second ed., Clarendon, Oxford, 1997.
- [37] M. Streckova, I. Batko, M. Batkova, R. Bures, M. Fabrova, R. Dzunda, H. Hadra, Imaging of magnetic domain structure in  $FeSi/Mn_{(0.8)}Zn_{(0.2)}Fe_2O_4$  composite using magnetic force microscopy, *Acta Phys. Pol. A* 131 (2017) 714.
- [38] P.T. Phong, P.H. Nam, D.H. Manh, I.J. Lee,  $Mn_{0.5}Zn_{0.5}Fe_2O_4$  nanoparticles with high intrinsic loss power for hyperthermia therapy, *J. Magn. Magn Mater.* 433 (2017) 76.
- [39] S.A. Ebrahimi, S.M. Masoudpanah, H. Amiri, M. Yousefzadeh, Magnetic properties of MnZn ferrite nanoparticles obtained by SHS and sol-gel autoxidation techniques, *Ceram. Int.* 40 (2014) 6713.
- [40] B. Chethan, H.G. Raj Prakash, Y.T. Ravikiran, S.C. Vijayakumari, C.H.V.V. Ramana, S. Thomas, D. Kim, Enhancing humidity sensing performance of polyaniline/water soluble graphene oxide composite, *Talanta* 196 (2019) 337–344.
- [41] K. Manjunatha, V. Jagadeesha Angadi, R.A.P. Ribeiro, M.C. Oliveira, S.R. de Lázaro, M.R.D. Bomio, S. Mattepanavar, S. Rayaprol, P.D. Babu, U. Mahaboob Pasha, Structural, Electronic and Magnetic properties of  $Sc^{3+}$  doped  $CoCr_2O_4$  nanoparticles, *New J. Chem.* 44 (2020) 14246–14255.
- [42] K. Manjunatha, V. Jagadeesha Angadi, K.M. Srinivasamurthy, Shidaling Mattepanavar, Vinayak K. Pattar, U. Mahaboob Pasha, Exploring the structural, dielectric and magnetic properties of 5 mol%  $Bi^{3+}$ -substituted  $CoCr_2O_4$  nanoparticles, *J. Supercond. Nov. Magnetism* 71 (2020) 1–12.
- [43] V. Jagadeesha Angadi, K. Manjunatha, N.H. Ayachit, Correlation of internal strain and size with electrical and magnetic properties of  $Ce^{3+}$ -doped manganese ferrimagnetic nanoparticles, *J. Mater. Sci. Mater. Electron.* 32 (2021) 9275–9293.
- [44] Mirza Mahmood Baig, Muhammad Asif Yousuf, Muhammad Farooq Warsi, Philips Olaleye Agboola, Muhammad Sher, Imran Shakir, Surfactant assisted synthesis of rare earth  $Dy^{3+}$ -substituted  $MnFe_2O_4$  nanoparticles, *Ceram. Int.* 45 (2019) 18014–18022.
- [45] K. Manjunatha, V. Jagadeesha Angadi, R. Rajaramakrishna, U. Mahaboob Pasha, Role of 5 mol% Mg-Ni on the structural and magnetic properties of cobalt chromates crystallites prepared by solution combustion technique, *J. Supercond. Nov. Magnetism* 33 (2020) 2861–2866.
- [46] V. Jagadeesha Angadi, K. Manjunatha, K. Praveena, Vinayak K. Pattar, Brian Jeevan Fernandes, S.O. Manjunatha, Jakeer Husain, S.V. Angadi, L. D. Horakeri, K.P. Ramesh, Magnetic properties of larger ionic radii samarium and gadalonium doped manganese zinc ferrite nanoparticles prepared by solution combustion method, *J. Magn. Magn Mater.* 529 (2021) 167899.
- [47] V. Jagadeesha Angadi, A.V. Anupama, R. Kumar, S. Mattepanavar, B. Rudraswamy, B. Sahoo, Observation of enhanced magnetic pinning in  $Sm^{3+}$ -substituted nanocrystalline Mn-Zn ferrites prepared by propellant chemistry route, *J. Alloys Compd.* 682 (2016) 263–274.
- [48] Jing Ren, Zhanxian Zhang, Xinxiu Ma, Yunbo Zhong, Jincang Zhang, Zhongming Ren, Yongsheng Liu, Tuning the structural and magnetic properties of MnZn nano-ferrites synthesized under a high magnetic field, *J. Magn. Magn Mater.* 495 (2020) 165832.
- [49] Q. Chen, M. Nie, Y. Guo, Controlled synthesis and humidity sensing properties of CdS/polyaniline composite based on CdAl layered double hydroxide, *Sensor. Actuator. B Chem.* 254 (2018) 30–35.
- [50] H. Farahani, R. Wagiran, M.N. Hamidon, Humidity sensors principle, mechanism, and fabrication technologies, A comprehensive review 14 (2014) 7881–7939.
- [51] B. Chethan, H.G.R. Prakash, Y.T. Ravikiran, S.C. Vijayakumari, S. Thomas, Polypyrrole based core-shell structured composite based humidity Sensor operable at room temperature, *Sensor. Actuator. B Chem.* 296 (2019) 126639.
- [52] H.R. LakshmiPrasanna, K. Manjunatha, V. Jagadeesha Angadi, U. Mahaboob Pasha, Jakeer Husain, Effect of cerium on structural, microstructural, magnetic and humidity sensing properties of Mn-Bi ferrites, *Nano-Struct. Nano-Objects* 24 (2020) 100608.
- [53] Y. Li, K. Fan, H. Ban, M. Yang, Detection of very low humidity using polyelectrolyte/graphene bilayer humidity sensors, *Sensor. Actuator. B Chem.* 222 (2016) 151–158.
- [54] A.T. Ramaprasad, V. Rao, Chitin-polyaniline blend as humidity sensor, *Sensor. Actuator. B Chem.* 148 (2010) 117–125.

- [55] Z. Chen, C. Lu, Humidity sensors: a review of materials and mechanisms, *Sens. Lett.* 3 (2005) 274–295.
- [56] K. Manjunatha, K.M. Srinivinasamurthy, C.S. Naveen, Y.T. Ravikiran, E.I. Sitalo, S. P. Kubrin, Siddaling Mattepanavar, N. Sivasankara Reddy, V. Jagadeesha Angadi, Observation of enhanced humidity sensing performance and structure, dielectric, optical and DC conductivity studies of scandium doped cobalt chromate, *J. Mater. Sci. Mater. Electron.* 30 (2019) 17202–17217.
- [57] D. Zhang, D. Wang, P. Li, X. Zhou, X. Zong, G. Dong, Facile fabrication of high-performance QCM humidity sensor based on layer-by-layer self-assembled polyaniline/graphene oxide nanocomposite film, *Sensor. Actuator. B Chem.* 255 (2018) 1869–1877.